6-20-2020

Flow simulation considering adsorption boundary layer based on digital rock and finite element method

Yong Fei Yang
China University of Petroleum (East China)

Ke Wang
China University of Petroleum (East China)

Qian Fei Lv
China University of Petroleum (East China)

Roohollah Askari
Michigan Technological University, raskari@mtu.edu

Qing Yan Mei
Southwestern Hospital Chongqing

See next page for additional authors

Follow this and additional works at: https://digitalcommons.mtu.edu/michigantech-p

Part of the Geological Engineering Commons, and the Mining Engineering Commons

Recommended Citation

Authors

Yong Fei Yang, Ke Wang, Qian Fei Lv, Roohollah Askari, Qing Yan Mei, Jun Yao, Jie Xin Hou, Kai Zhang, Ai Fen Li, and Chen Chen Wang

Flow simulation considering adsorption boundary layer based on digital rock and finite element method

Yong-Fei Yang[1,2] · Ke Wang[1,2] · Qian-Fei Lv[1,2] · Roohollah Askari[3] · Qing-Yan Mei[4] · Jun Yao[1,2] · Jie-Xin Hou[5] · Kai Zhang[1,2] · Ai-Fen Li[1,2] · Chen-Chen Wang[6]

Abstract

Due to the low permeability of tight reservoirs, throats play a significant role in controlling fluid flow. Although many studies have been conducted to investigate fluid flow in throats in the microscale domain, comparatively fewer works have been devoted to study the effect of adsorption boundary layer (ABL) in throats based on the digital rock method. By considering an ABL, we investigate its effects on fluid flow. We build digital rock model based on computed tomography technology. Then, microscopic pore structures are extracted with watershed segmentation and pore geometries are meshed through Delaunay triangulation approach. Finally, using the meshed digital simulation model and finite element method, we investigate the effects of viscosity and thickness of ABL on microscale flow. Our results demonstrate that viscosity and thickness of ABL are major factors that significantly hinder fluid flow in throats.

Keywords Digital rock · Low-permeability rocks · CT technology · Adsorption boundary layer · Numerical simulation · Finite element method

Edited by Yan-Hua Sun

✉ Yong-Fei Yang
yangyongfei@upc.edu.cn

1 Key Laboratory of Unconventional Oil and Gas Development (China University of Petroleum (East China)), Ministry of Education, Qingdao 266580, Shandong, People's Republic of China

2 Research Center of Multiphase Flow in Porous Media, School of Petroleum Engineering, China University of Petroleum (East China), Qingdao 266580, Shandong, People's Republic of China

3 Department of Geological and Mining Engineering and Sciences, Michigan Technological University, Houghton, MI, USA

4 Exploration and Development Research Institute of PetroChina Southwest Oil and Gas Field Company, Chengdu 610041, Sichuan, People's Republic of China

5 School of Materials Science and Engineering, Beihang University, Beijing 100191, People's Republic of China

6 Hubei Cooperative Innovation Center of Unconventional Oil and Gas, Yangtze University, Wuhan 430100, Hubei, People's Republic of China

List of symbols

A	Cross-sectional area of porous media, μm^2
A_r	The ratio of cross-sectional area of adsorption boundary region to the total cross-sectional area of throat
h_r	Relative thickness of the ABL, dimensionless
h	ABL thickness, μm
k	Permeability of porous media, μm^2
Δp	Pressure difference across the porous media, Pa
Q_0	Outlet flow rate without the influence of ABL, $\mu m^3/s$
Q_{sim}	Outlet flow rate under the influence of ABL, $\mu m^3/s$
r_0	Throat radius, μm
μ_r	Relative viscosity of ABL, dimensionless
μ	Average viscosity of total fluid in a throat, mPa·s
μ_1	ABL viscosity, mPa·s
μ_2	Viscosity of bulk fluid, mPa·s

1 Introduction

Low-permeability (< 50 mD) oil and gas reservoirs are being widely considered by the oil and gas exploration and development in recent years (Sun et al. 2017). Compared to conventional reservoirs, pores and throats in low-permeability

reservoirs are narrow (Sun et al. 2015; Zhang et al. 2018a; Huang et al. 2018) and have a large specific surface (Xiong et al. 2009). When fluid flows in a low-permeable porous media, the non-Darcy flow will occur, and there will be a pseudo-threshold pressure gradient (Lei et al. 2008; Zeng et al. 2011). Huang (1998) proposed that the existence of boundary fluid can explain the physical nonlinear phenomenon. In a porous media, liquid molecules concentrated on the surface of pores result in a boundary region with higher fluid viscosity and form a stagnant liquid layer that is called adsorption boundary layer (ABL) (Fig. 1), which is one of the main reasons for the occurrence of nonlinear flow (Huang 1998; Song et al. 2010; Huang et al. 2013; Yang et al. 2020c). The mechanism of pseudo-threshold pressure gradient can be interpreted by the molecular interaction theory and ABL theory (Xiong et al. 2009; Li et al. 2015b; Shen et al. 2019). In porous media, fluid viscosity is influenced by the ABL (Song et al. 2016). The physicochemical properties of crude oil affect the viscosity and thickness of this layer (Li et al. 2011; Tian et al. 2015; Guo et al. 2015). Li et al. (2018) built a capillary permeability model and studied the influence of ABL on tight reservoirs. Yang et al. (2018) studied the ABL in the plate space using nuclear magnetic resonance. Song et al. (2019a) proposed a new single-channel flow model for describing nonlinear flow in low-permeability reservoirs based on ABL theory. Most of previous studies (Li et al. 2015a; Tian et al. 2016; Chen et al. 2018) investigated the effect of ABL on fluid flow in a single pipe, whereas real porous media are more complicated. Therefore, it is of great significance to study the influence of ABL by considering more complex and realistic porous media. The inner structure of rocks, in micro- and nanoscales, can be revealed through high-resolution imaging techniques such as focused ion beam scanning electron microcopy (FIB-SEM) (Desbois et al. 2008, 2011; Li et al. 2015c) and computed tomography (CT) (Coles et al. 1998;
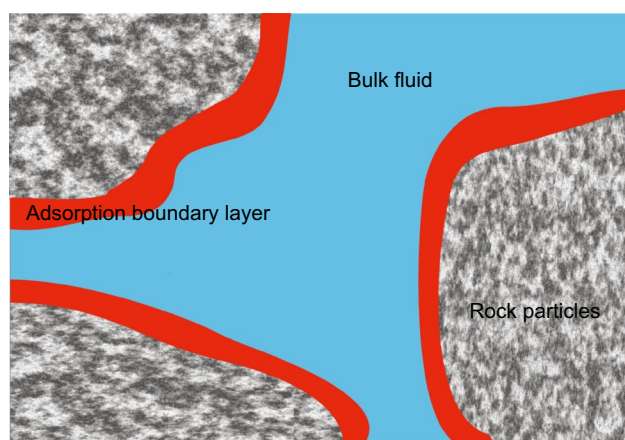
Schembre and Kovscek 2003; Shabaninejad et al. 2018; Yang et al. 2020a, b).

In this study, we investigate the effects of thickness and viscosity of ABL on fluid flow in porous media by constructing digital rock models using the CT scanning method. Pore geometries are extracted from real rock samples, and Delaunay triangulation algorithm is utilized to generate finite element grids, which is explained in Sect. 2 (Lee and Schachter 1980; Shewchuk 2002). The fluid flow simulation considering a stagnant ABL for digital rock is performed using Navier–Stokes (N–S) equations. Because it is difficult to derive formulations to calculate the ABL thickness theoretically, and even more challenging to define the existence of ABL directly in the numerical simulations, an indirect approach is employed to study the absorption boundary layer. In this work, we calculate an average viscosity of fluid by considering viscosity and thickness of ABL. The flow behavior of digital rock models under the effect of ABL is discussed for different rock samples.

2 Reconstruction of geometric model

According to different physical characteristics, four core samples are selected to study the effect of ABL. Berea sandstone, which has a high degree of homogeneity, is used as standard stone to compare the calculation results. The sandstone samples 1, 2 and 3 are from low-permeability formations in Shengli oil field. Samples 1–3 have been selected because they have different pore structures, and thus, we could gain a better understating of the effect of ABL on fluid flow with respect to different pore configurations.

The CT scanning technique provides a nondestructive way to image internal structures of a rock sample (Shabaninejad et al. 2018; Song et al. 2019b). In this study, the instrument used for X-ray CT scanning is Zeiss Versa Micro-XCT-400. Its minimum spatial resolution is 0.35 μm, the view pixel is 2048^2, and the focus size is 5 μm. The resolution of samples 1–3 from Shengli oil field is 3.7594 μm, and the Berea sandstone downloaded from (Dong and Blunt 2009) is 5.345 μm.

The CT scanning yields a three-dimensional (3D) gray image for each sample. Prior to segmentation, for image enhancement, we apply a non-local means filter to enhance the signal-to-noise ratio (Buades et al. 2005). Thereafter, we use the watershed segmentation method to the filtered image to convert grayscale image into two phases (pore and matrix) so that the resulted pore structures can be used for geometric modeling (Saarinen 1994). The pore structures of digital core samples are shown in Fig. 2. The size of samples is $150 \times 150 \times 150$ pixel^3.

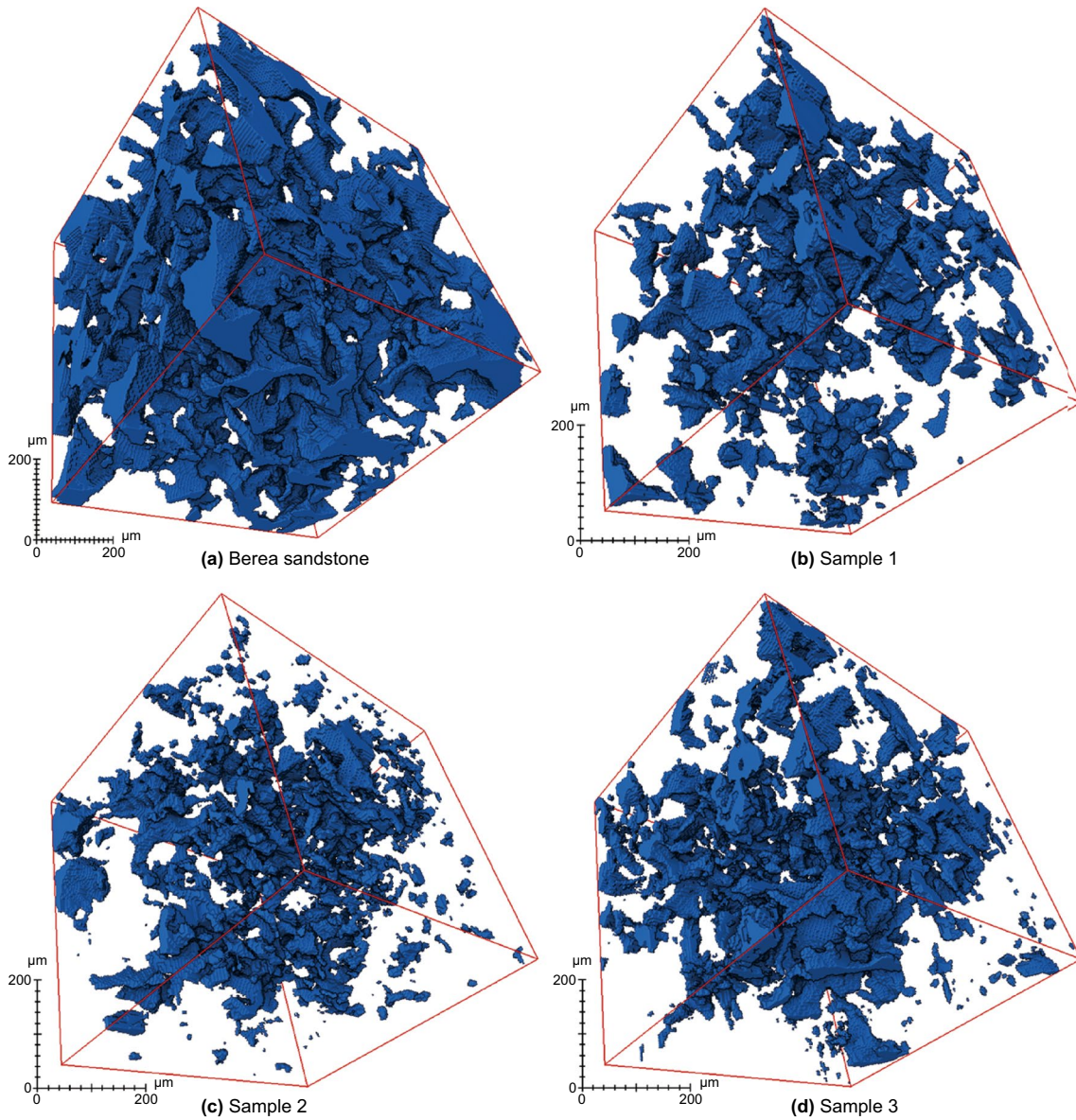**Fig. 1** Diagrammatic sketch of adsorption boundary layer (ABL)

Fig. 2 3D pore structures of digital core samples

The main parameters of these core samples are presented in Table 1. The porosities of samples are calculated based on reconstructed digital rock with Avizo software, and permeabilities are estimated through flow simulation using Lattice Boltzmann method (Qian et al. 1992; Ren et al. 2015; Zhang et al. 2019). By adopting the pore network model, we obtain the average radius (Yang et al. 2015, 2019; An et al. 2016).

Table 1 Parameters of sandstone core samples

Core sample	Porosity, %	Permeability, mD	Average pore radius, μm	Average throat radius, μm	Average total radius, μm
Berea sandstone	11.98	1765.08	17.48	12.63	14.02
Sample 1	7.93	6.80	10.42	7.29	8.46
Sample 2	5.53	3.47	8.89	6.23	7.26
Sample 3	7.00	5.37	9.11	6.36	7.42

For low-permeability sandstones, pore structure characteristics play an important role in flow mechanism. Therefore, the pore structure of the digital rock sample is characterized by extracting a pore network model (Dong and Blunt 2009; Wang et al. 2020). From Fig. 3a, the pore radius of samples 1, 2 and 3 have a range mainly within 20 μm. From Fig. 3b, we note that the throat radius of Berea sandstone is generally larger than those of samples 1, 2 and 3. In addition, the throat radius of samples 1, 2 and 3 range less than 10 μm. The peak values of pore and throat radius distribution curve of Berea sandstone are larger than that of three low-permeability samples. This indicates that low-permeability sandstone samples are mainly composed of pores and throats with smaller size.

We discretize the geometrically complex flow domain of a binary model using unstructured mesh and simulate fluid flow using the finite element method (FEM) (Madadi and Saadatfar 2017). A high mesh density is assigned to the target areas to capture the effects of the adsorption layer at narrower pore throats. Figure 2 shows pore structures of Berea sandstone sample and samples 1–3 with isolated pores. Since isolated pores have no contribution to the fluid flow, before meshing the geometry, they are removed to reduce the computational load. We use Delaunay triangulation approach, a typical surface rendering method, to mesh the geometry (Shewchuk 2002; Fabri and Pion 2009). And, we put a 3D image array of 0 and 1 without isolated pores into Iso2Mesh generator to form finite element grids (Fang and Boas 2009). In the process of modeling, we optimize the quality of the target model by adjusting the model parameters, which is easy to maintain the authenticity of model to a maximum extent. The results of pore structure meshing are shown in

Table 2 Elements of meshing results about pore geometry

	Berea sandstone	Sample 1	Sample 2	Sample 3
Number of nodes	1371630	233809	204540	233325
Number of elements	6007804	1012105	876968	993512

Table 2 and Fig. 4. The resulted grid file is imported into COMSOL Multiphysics software for flow simulation in the *z* direction.

3 Numerical simulation of flow considering the ABL effects

3.1 Flow equations and model establishment

Fluid flow in unconventional low-permeable rocks is influenced by confinement effect, and the applicability of flow equations should be discussed (Bahukudumbi and Beskok 2003; Barber and Emerson 2006; Zhang et al. 2012; Yao et al. 2013). Nanoscale liquid flow behavior was investigated by molecular dynamic simulations and nanofluidic experiments, which demonstrated that the continuity assumption is valid at nanoscale when the size of flow channel exceeds several nanometers (Sparreboom et al. 2010; Wang et al. 2016; Wu et al. 2017; Zhang et al. 2018b). In this paper, we only consider liquid phase, and the pore and throat sizes are in the micrometer scale (as shown in Fig. 3); therefore, the continuity assumption is reasonable and N–S equations are applicable.
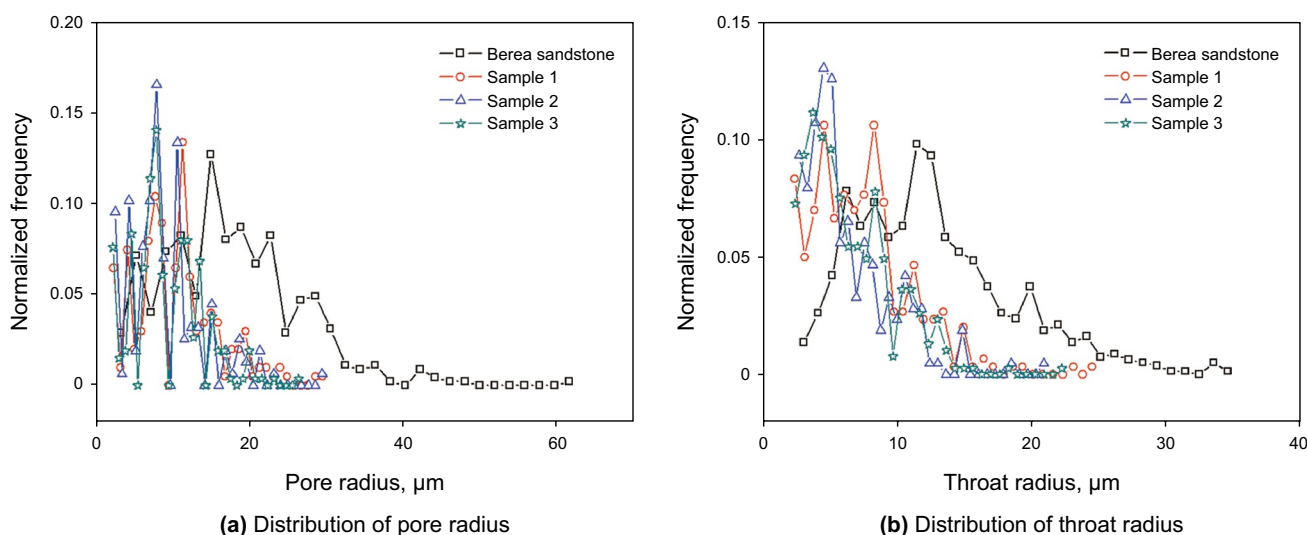

(a) Distribution of pore radius

(b) Distribution of throat radius

Fig. 3 Distribution of **a** pore and **b** throat radius of the samples obtained from pore network model

(a) Berea sandstone
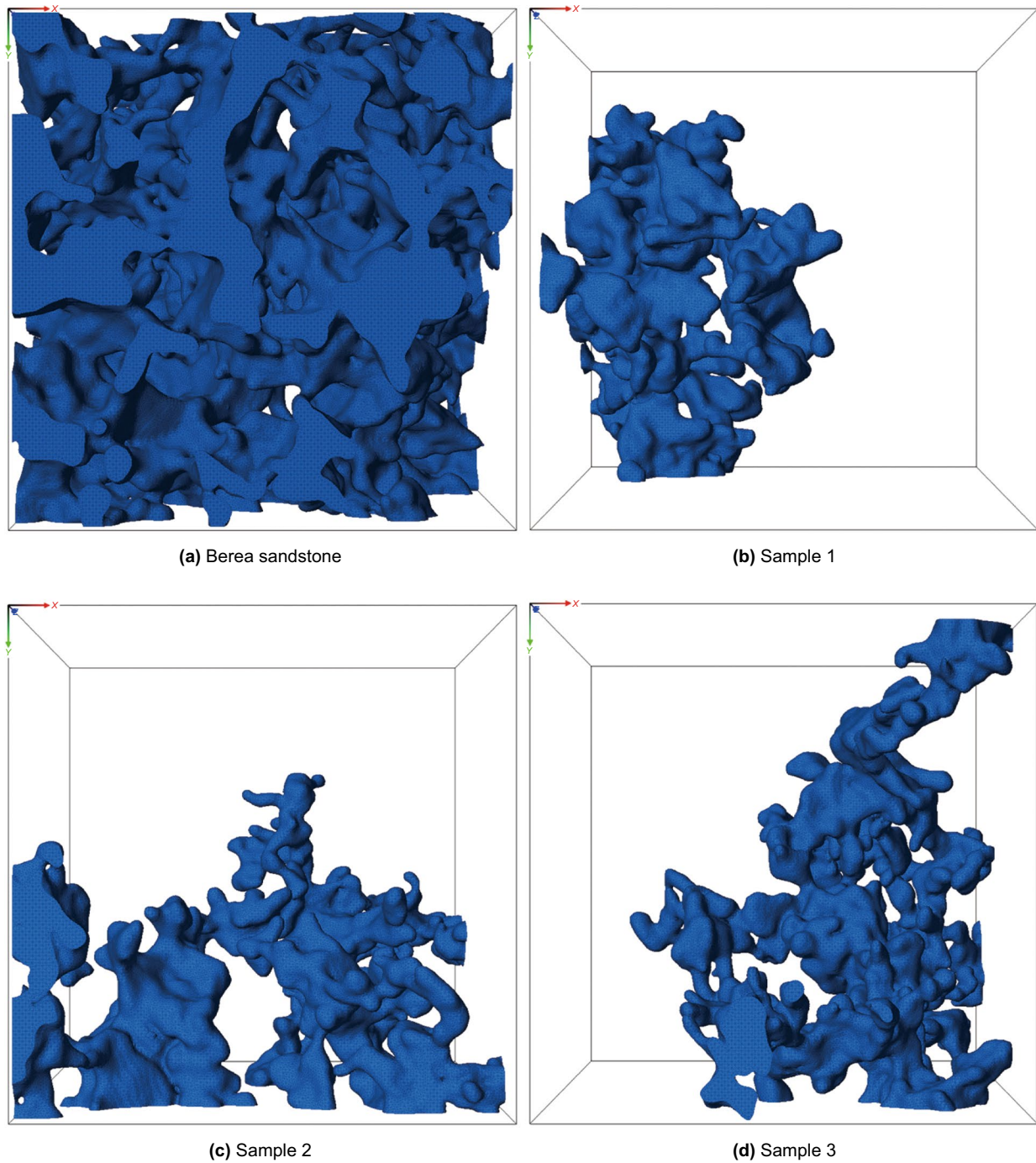
(b) Sample 1

(c) Sample 2

(d) Sample 3

Fig. 4 Meshing results of pore structure without isolated pores. Isolated pores are removed to reduce computational load. Connected pore structure after meshing is used to simulate the flow

We assume that the fluid flow in porous media is continuous and incompressible. When the gravity is neglected, the N–S equations can be expressed as follows:

$$\frac{d\vec{u}}{dt} = -\frac{1}{\rho}\nabla p + \frac{\mu}{\rho}\nabla^2\vec{u} \tag{1}$$

where $\vec{u}$ is flow velocity and ρ is density. According to Huang's conclusion (Huang 1998; Huang et al. 2013), we expect that the fluids in both low-permeable samples (samples 1, 2 and 3) and Berea sandstone sample follow the laminar flow. Therefore, we adopt laminar flow pattern to

simulate the fluid flow at a pressure difference of 7.5 Pa and a fluid density of 998.3 kg/m^3.

3.2 Simulation results of models without ABL

In order to study the effect of ABL in different samples, flow simulation is performed before and after considering the boundary layer. The velocity fields of models without existence of ABL are shown in Fig. 5, from which we observe the fluid flows mainly in a relatively short path between the inlets and outlets. In addition, we note that the pores with smaller radius have faster velocities. In general, the velocity becomes minimum near the throat wall whereas maximum at the throat center. Therefore, the velocity increases gradually from the surface to the center of the throat.

3.3 Influence of ABL viscosity and thickness

We define dimensionless thickness and viscosity as:

$$h_{\rm r} = \frac{h}{r_0}, \ \mu_{\rm r} = \frac{\mu_1}{\mu_2} \tag{2}$$

where $h_{\rm r}$, h, r_0 are the relative thickness of ABL, ABL thickness, and throat radius, respectively; $\mu_{\rm r}$, μ_1, μ_2 are the relative viscosity of ABL, ABL viscosity and bulk fluid viscosity, respectively. The viscosity of fluid in a throat can be calculated by Huang (1998):

$$\mu = A_{\rm r}\mu_1 + (1 - A_{\rm r})\mu_2. \tag{3}$$

The ratio of the cross-sectional area of adsorption boundary region to the total cross-sectional area of throat is (Huang 1998; Huang et al. 2013):
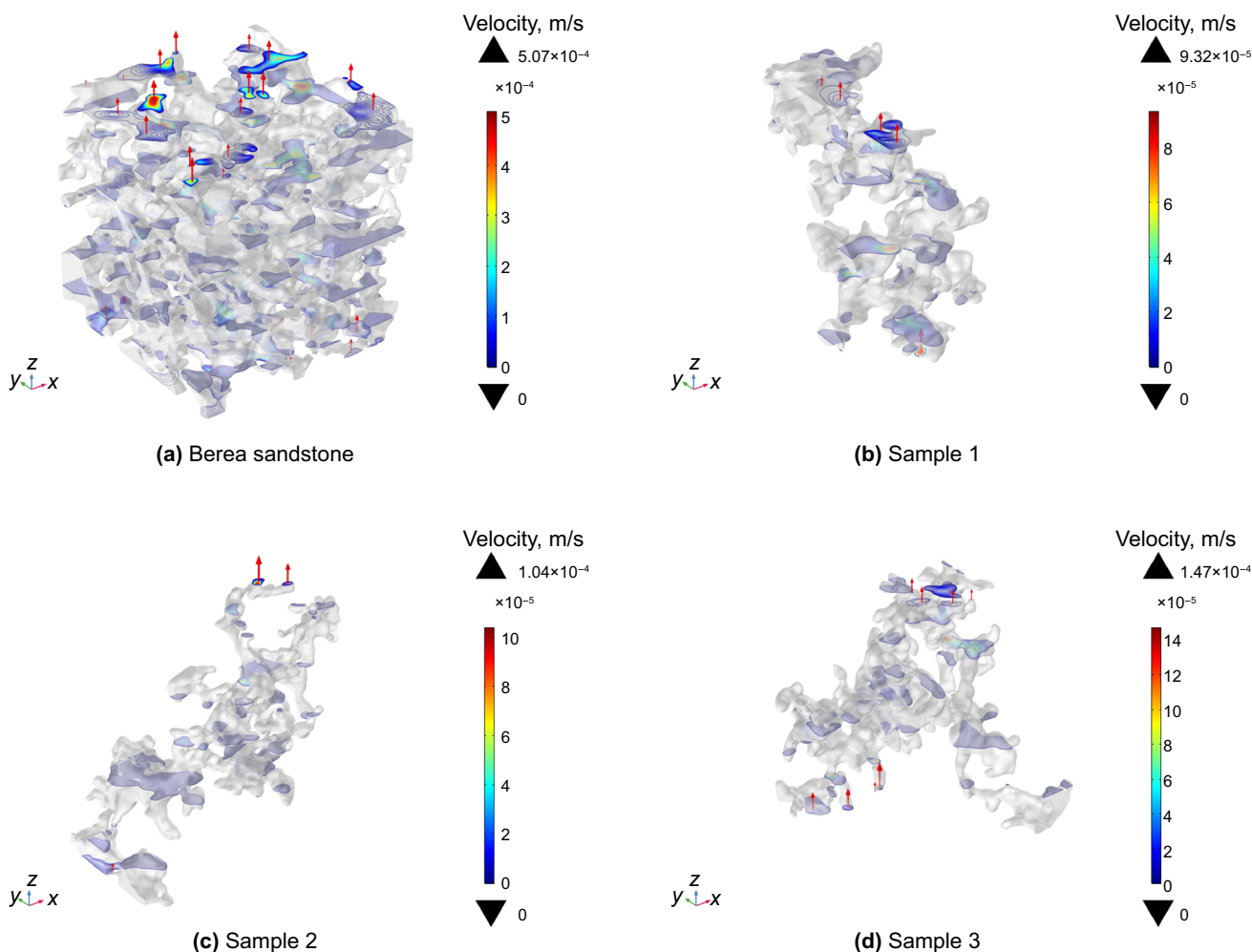

(a) Berea sandstone

(b) Sample 1

(c) Sample 2

(d) Sample 3

Fig. 5 Global slice diagrams of velocity field in different samples without ABL. The legend represents the range of velocity on global slice. The red arrows indicate flow direction. The fluid flows in the *z* direction

$$A_r = 2\frac{h}{r_0} - \left(\frac{h}{r_0}\right)^2. \tag{4}$$

Given different values of h and μ_r, μ can be calculated from Eq. (3). The ABL thickness and viscosity remain constant during our flow simulations. Here, we assume that μ_2 is 1 mPa·s; therefore, the value of μ_r is equal to μ_1. In order to quantify the influence of adsorption layer thickness and viscosity, we assume that the range of h is 0–3 μm and μ_r is 2–10, respectively.

By assuming the thickness of ABL is constant, we investigate the effect of ABL viscosity on the microscopic fluid flow in porous media. The velocity fields of our models with consideration of ABL (h is 0.2 μm, μ_r is 5) are shown in Fig. 6. Taken the influence of ABL into account, the flow velocities in all samples are generally lower compared with those simulation results without ABL.

In this paper, when ABL is considered for a given thickness and viscosity, the outlet flow rate is denoted by Q_{sim}, whereas the flow rate without ABL is expressed as Q_0. And Q_{sim}/Q_0 is used to quantitatively analyze the effect of ABL thickness and viscosity. For instance, $Q_{sim}/Q_0 = 1$ means that no ABL is considered.

From Figs. 7, 8, 9 and 10, with an increase in ABL viscosity, the simulated flow rate decreases and the absolute value of the slope increases. When the viscosity of ABL is low, the initial relationship between Q_{sim}/Q_0 and ABL thickness is approximately linear. However, as the viscosity of ABL increases, the data points gradually deviate from the straight line, presenting a nonlinear relationship. As the viscosity of ABL increases, the drop of Q_{sim}/Q_0 slows down at the same ABL thickness, which indicates the influence of ABL viscosity on fluid flow is limited to a certain extent. The relationships between Q_{sim}/Q_0 and ABL thickness of samples 1–3 show more nonlinear behavior than the Berea sandstone sample, which indicates the thickness
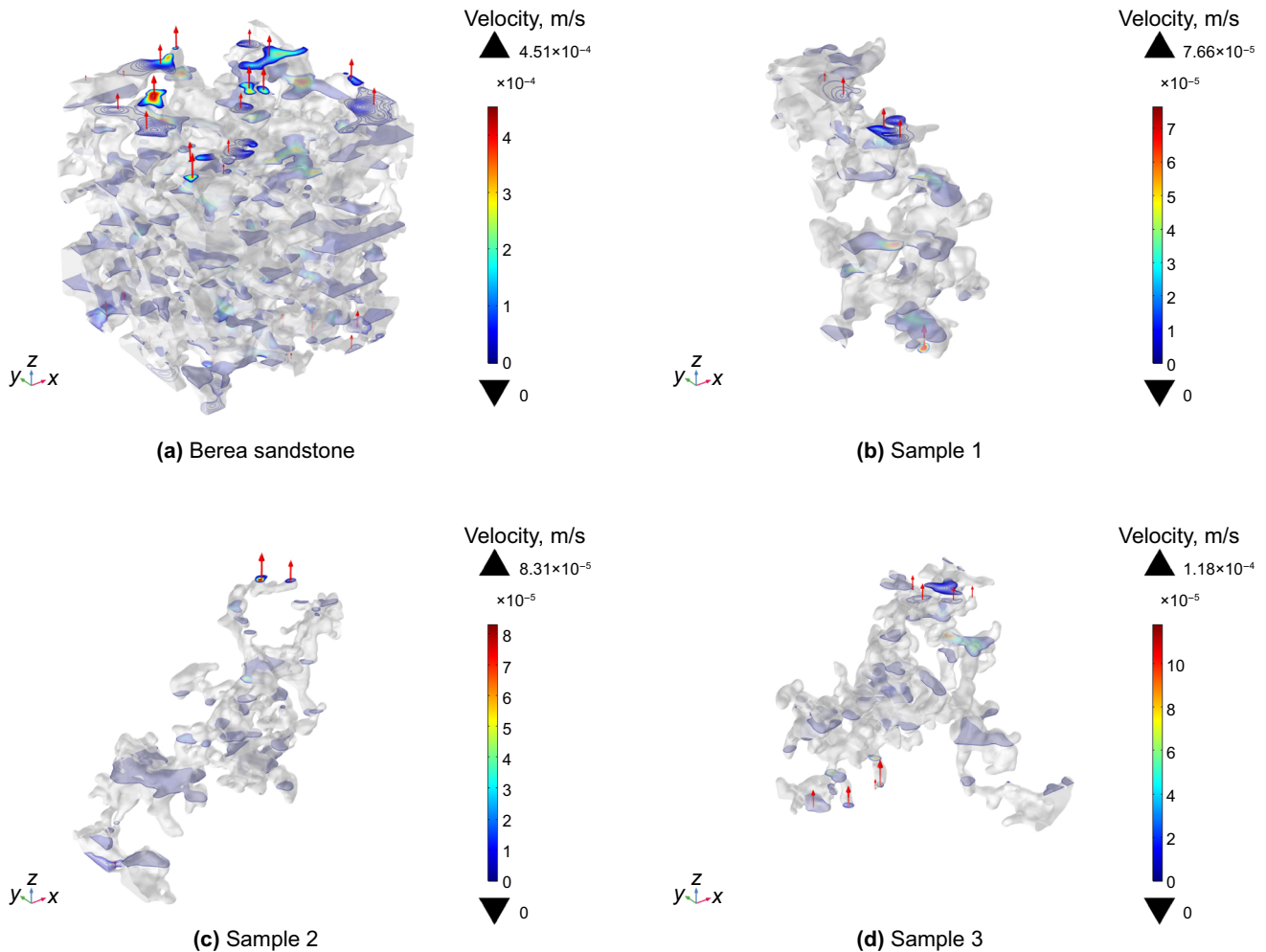

Fig. 6 Global slice diagrams of velocity field in different samples with ABL. (h is 0.2 μm, μ_r is 5.) The legend represents the range of velocity on global slice. The red arrows indicate flow direction. The fluid flows in the z direction
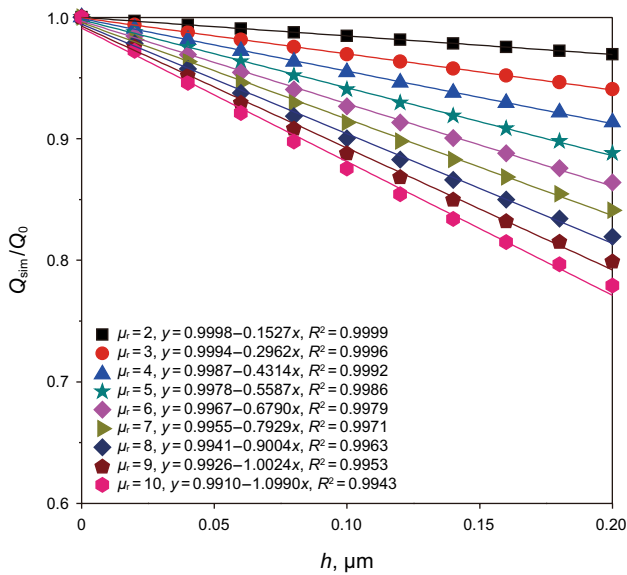
Fig. 7 Influence of ABL thickness (0–0.2 μm) on fluid flow in the Berea sandstone sample under different ABL viscosities
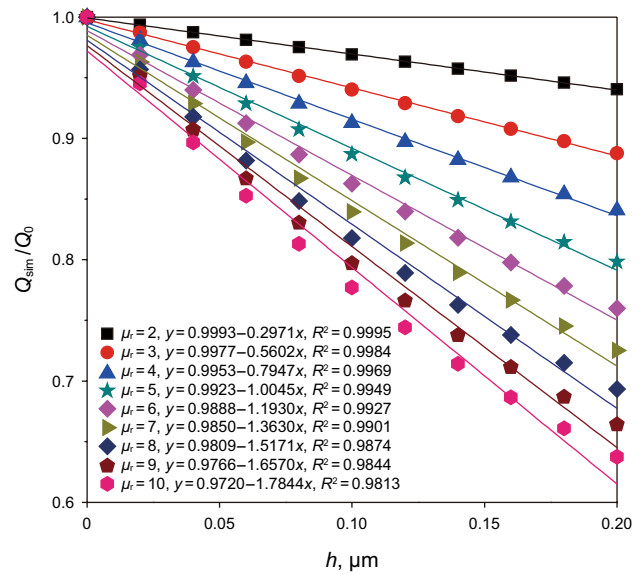

Fig. 9 Influence of ABL thickness (0–0.2 μm) on fluid flow in sandstone sample 2 under different ABL viscosities
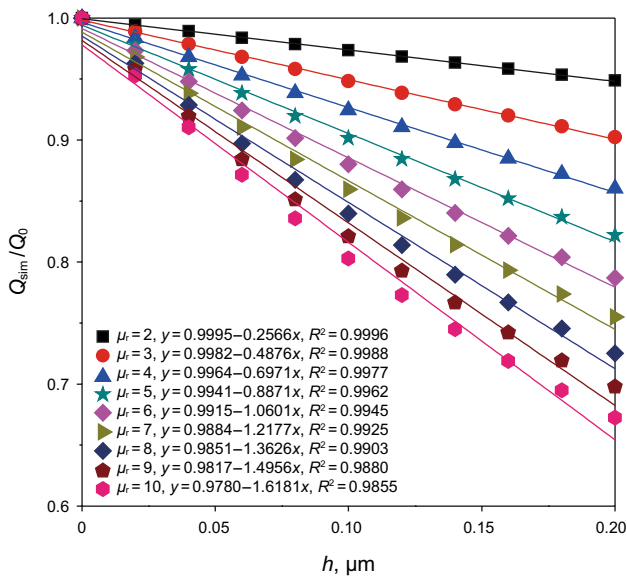

Fig. 8 Influence of ABL thickness (0–0.2 μm) on fluid flow in sandstone sample 1 under different ABL viscosities
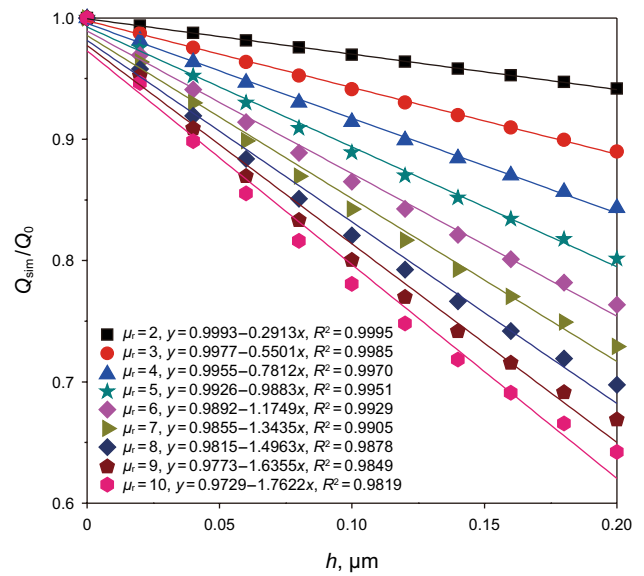

Fig. 10 Influence of ABL thickness (0–0.2 μm) on fluid flow in sandstone sample 3 under different ABL viscosities

and viscosity of ABL have a more significant effect on low-permeability porous media, and this is mainly caused by the larger pore radius and better connectivity in the Berea sandstone sample compared with samples 1–3.

Figure 11 shows the slope values of fitting curves in Figs. 7, 8, 9 and 10 that are plotted as a function of the relative viscosity of ABL. Note that for a given viscosity, the low-permeable samples have higher absolute slope values compared to the Berea sandstone sample, which indicates

that the thickness and viscosity of ABL have greater influence on low-permeability rocks. This observation is consistent with the characteristics of the throat radius shown in Fig. 3b in which the throat radius of samples 1–3 is generally lower compared with those of the Berea sandstone sample. Due to the smaller size of throat radius in low-permeable rocks, when the thickness and viscosity of ABL increase slightly, the flow resistance increases significantly, which results in a lower flow rate at the same pressure gradient.
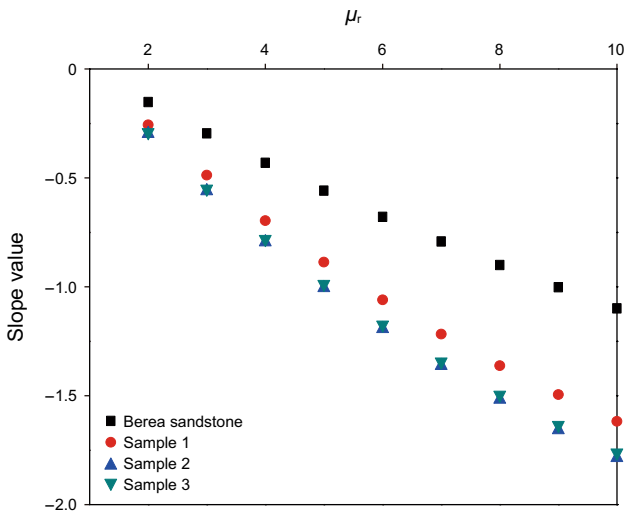
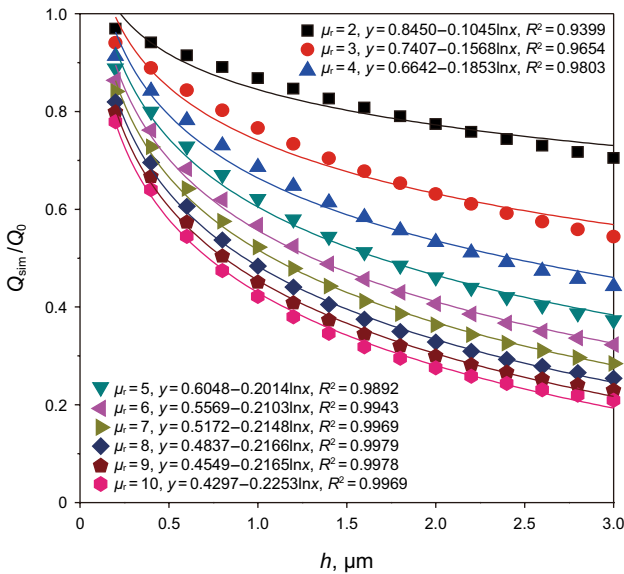**Fig. 11** Slope values of fitting curves in Figs. 7, 8, 9 and 10

Fig. 12 Influence of ABL thickness (0–3 μm) on fluid flow in the Berea sandstone sample under different ABL viscosities

Fig. 13 Influence of ABL thickness (0–3 μm) on fluid flow in sandstone sample 1 under different ABL viscosities

Fig. 14 Influence of ABL thickness (0–3 μm) on fluid flow in sandstone sample 2 under different ABL viscosities

Figures 12, 13, 14 and 15 show the effects of wide-ranged ABL thickness for given ABL viscosities on microscale flow of Berea sandstone and samples 1–3, respectively. We note that for a given ABL viscosity, there is a logarithmic relationship between ABL thickness and Q_{sim}/Q_0. As the thickness increases, the decline trend of Q_{sim}/Q_0 becomes slower. For a given ABL thickness, as the ABL viscosity increases, the downtrend of Q_{sim}/Q_0 slows down gradually. Our simulation results demonstrate that the increase in ABL viscosity and thickness lead to stronger flow resistance and significantly hinder liquid flow in pore throats.
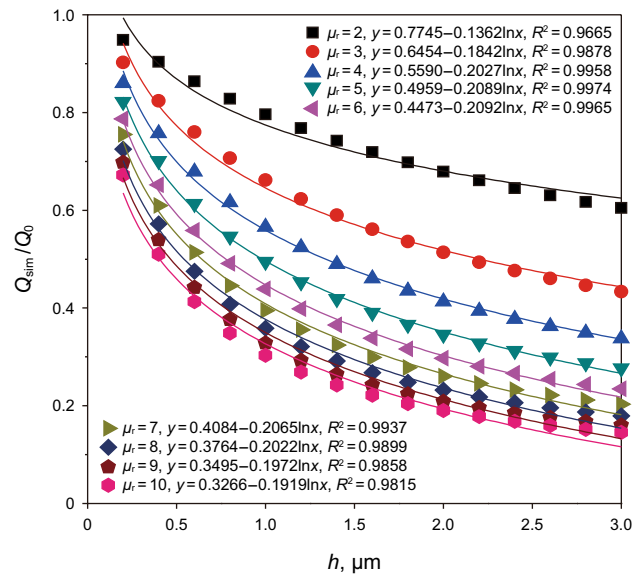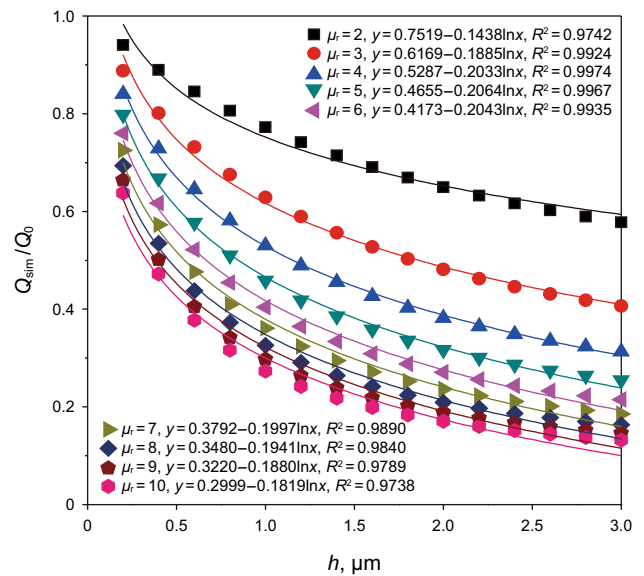
3.4 Effects of ABL on fluid flow in different rock samples

In order to investigate the influence of pore space structure on flow behavior, the simulated flow rates under the effect of ABL for Berea sandstone and low-permeable rock samples are presented in Figs. 16 and 17. Firstly, we assume that the absolute thickness of ABL is a constant value of 0.2 μm and calculate flow rates for different rock samples (Fig. 16).
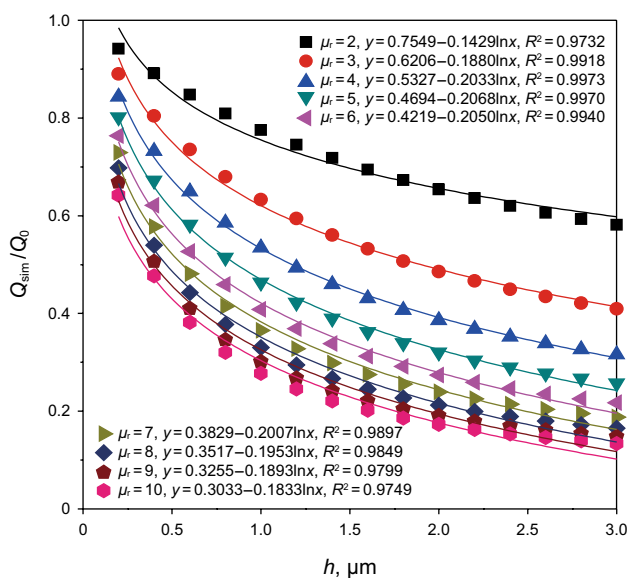
Fig. 15 Influence of ABL thickness (0–3 μm) on fluid flow in sandstone sample 3 under different ABL viscosities
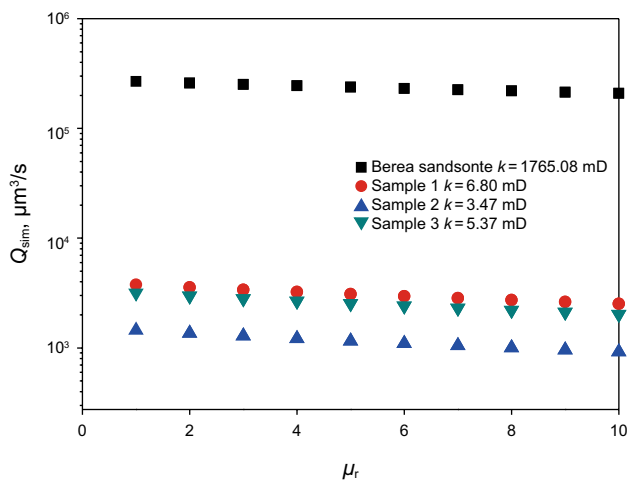

Fig. 16 Influence of relative viscosity of ABL on simulated flow rate for different rock samples

Secondly, the relative viscosity of ABL is also assumed to be a constant ($\mu_r = 2$); then, the relationships between flow rate and absolute ABL thickness are obtained (Fig. 17).

As shown in Figs. 16 and 17, when the thickness and viscosity of ABL increase, the flow rates of all samples get smaller. The flow rate of the Berea sandstone sample is about 100 times larger than that of the other three samples and less
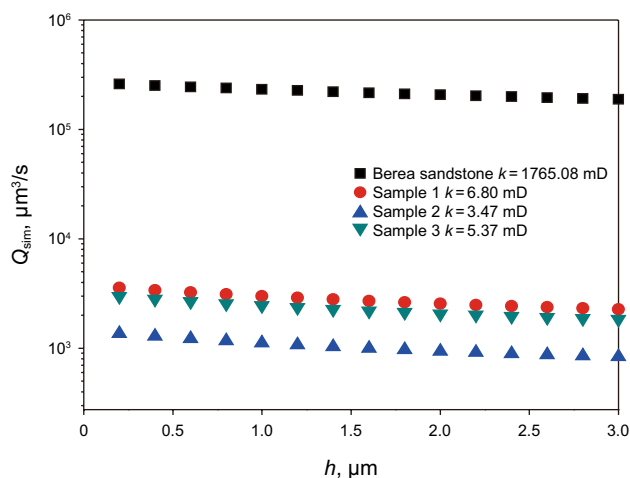

Fig. 17 Influence of ABL thickness on simulated flow rate for different rock samples

influenced by ABL thickness and viscosity. In comparison, for samples 1–3 with ultra-low permeability, the flow rate remains within a very small scale and becomes more sensitive to ABL. Therefore, in low- and ultra-low-permeability rocks, the existence of the ABL will cause great damage to the effective development of reservoirs.

4 Conclusions

The microscale model of porous media based on CT and digital rock analysis can reflect the real pore structure of rocks. Therefore, it can be used to simulate the influence of adsorption boundary layer. Using the digital rock constructed by CT scanning, we meshed finite element grids and performed numerical simulation to study the effect of ABL viscosity and thickness on fluid flow for different rock samples.

With respect to our results, when the viscosity and thickness of ABL are small, the relationship between decrease in flow rate and increase in ABL thickness is approximately linear. On the contrary, it tends to be a nonlinear relationship. The effect of ABL thickness and viscosity for low-permeability porous media is more significant than Berea sandstone. It is due to larger pore radius and better connectivity in Berea sandstone. Compared with conventional reservoirs, the existence of ABL in low-permeability reservoirs causes more damage to reservoirs and makes oil development more difficult.

References

An SY, Yao J, Yang YF, Zhang L, Zhao JL, Gao Y. Influence of pore structure parameters on flow characteristics based on a digital rock and the pore network model. J Nat Gas Sci Eng. 2016;31:156–63. https://doi.org/10.1016/j.jngse.2016.03.009.

Bahukudumbi P, Beskok A. A phenomenological lubrication model for the entire Knudsen regime. J Micromech Microeng. 2003;13(6):873–84. https://doi.org/10.1088/0960-1317/13/6/310.

Barber RW, Emerson DR. Challenges in modeling gas-phase flow in microchannels: from slip to transition. Heat Transfer Eng. 2006;27(4):3–12. https://doi.org/10.1080/01457630500522271.

Buades A, Coll B, Morel J. A non-local algorithm for image denoising. In: 2005 IEEE computer society conference on computer vision and pattern recognition (CVPR'05); 2005. p. 60–5. https://doi.org/10.1109/CVPR.2005.38.

Chen MQ, Cheng LS, Cao RY, Lyu CH. A study to investigate fluid–solid interaction effects on fluid flow in micro scales. Energies. 2018;11(9):2197. https://doi.org/10.3390/en11092197.

Coles ME, Hazlett RD, Spanne P, Soll WE, Muegge EL, Jones KW. Pore level imaging of fluid transport using synchrotron X-ray microtomography. J Pet Sci Eng. 1998;19(1):55–63. https://doi.org/10.1016/S0920-4105(97)00035-1.

Desbois G, Urai JL, Burkhardt C, Drury MR, Hayles M, Humbel B. Cryogenic vitrification and 3D serial sectioning using high resolution cryo-FIB SEM technology for brine-filled grain boundaries in halite: first results. Geofluids. 2008;8(1):60–72. https://doi.org/10.1111/j.1468-8123.2007.00205.x.

Desbois G, Urai JL, Kukla PA, Konstanty J, Baerle C. High-resolution 3D fabric and porosity model in a tight gas sandstone reservoir: a new approach to investigate microstructures from mm- to nm-scale combining argon beam cross-sectioning and SEM imaging. J Pet Sci Eng. 2011;78(2):243–57. https://doi.org/10.1016/j.petrol.2011.06.004.

Dong H, Blunt MJ. Pore-network extraction from micro-computerized-tomography images. Phys Rev E Stat Nonlinear Soft Matter Phys. 2009;80(3):036307. https://doi.org/10.1103/physreve.80.036307.

Fabri A, Pion S. CGAL: the computational geometry algorithms library. In: Proceedings of the 17th ACM SIGSPATIAL international conference on advances in geographic information systems; 2009. p. 538–9. https://doi.org/10.1145/1653771.1653865.

Fang QQ, Boas D. Tetrahedral mesh generation from volumetric binary and grayscale images. In: 2009 IEEE international symposium on biomedical imaging: from nano to macro; 2009. p. 1142–5. https://doi.org/10.1109/ISBI.2009.5193259.

Guo H, Wang FY, Li YQ, Yu ZY, Gao X, Gu YY, et al. Progress on flow mechanism in low permeability formation. Procedia Eng. 2015;126:466–70. https://doi.org/10.1016/j.proeng.2015.11.284.

Huang SY, Wu YY, Meng XB, Liu LW, Ji W. Recent advances on microscopic pore characteristics of low permeability sandstone reservoirs. Adv Geo-Energy Res. 2018;2(2):122–34. https://doi.org/10.26804/ager.2018.02.02.

Huang YZ. Porous flow mechanism of low permeability reservoir. Beijing: Petroleum Industry Press; 1998 **(in Chinese)**.

Huang YZ, Yang ZM, He Y, Wang XW. An overview on nonlinear porous flow in low permeability porous media. Theor Appl Mech Lett. 2013;3(2):022001. https://doi.org/10.1063/2.1302201.

Lee DT, Schachter BJ. Two algorithms for constructing a Delaunay triangulation. Int J Comput Inf Sci. 1980;9(3):219–42. https://doi.org/10.1007/BF00977785.

Lei Q, Xiong W, Yuan JR, Gao SS, Wu YS. Behavior of flow through low-permeability reservoirs. In: Europec/EAGE conference and exhibition. Society of Petroleum Engineers, 2008. https://doi.org/10.2118/113144-MS.

Li G, Ren WX, Meng YF, Yi F, Sun AS, Chu HZ. Boundary effect on liquid invasion in tight gas reservoirs. Therm Sci. 2015a;19(4):1393–6. https://doi.org/10.2298/TSCI1504393L.

Li HB, Guo HK, Yang ZM, Wang XW, Sun YP, Xu HC, et al. Boundary retention layer influence on permeability of tight reservoir. J Pet Sci Eng. 2018;168:562–8. https://doi.org/10.1016/j.petrol.2018.05.019.

Li JJ, Yan XT, Wang WM, Zhang YN, Yin JX, Lu SF, et al. Key factors controlling the gas adsorption capacity of shale: a study based on parallel experiments. Appl Geochem. 2015b;58:88–96. https://doi.org/10.1016/j.apgeochem.2015.03.009.

Li JJ, Yin JX, Zhang YN, Lu SF, Wang WM, Li JB, et al. A comparison of experimental methods for describing shale pore features—a case study in the Bohai Bay Basin of eastern China. Int J Coal Geol. 2015c;152:39–49. https://doi.org/10.1016/j.coal.2015.10.009.

Li Y, Lei Q, Liu XG, Xiao HM. Characteristics of micro scale nonlinear filtration. Pet Explor Dev. 2011;38(3):336–40. https://doi.org/10.1016/S1876-3804(11)60036-0.

Madadi M, Saadatfar M. A finite-element study of the influence of grain contacts on the elastic properties of unconsolidated sandstones. Int J Rock Mech Min Sci. 2017;93:226–33. https://doi.org/10.1016/j.ijrmms.2017.02.008.

Qian YH, D'Humières D, Lallemand P. Lattice BGK models for Navier–Stokes equation. Europhys Lett. 1992;17(6):479–84. https://doi.org/10.1209/0295-5075/17/6/001.

Ren JJ, Guo P, Guo ZL, Wang ZH. A Lattice Boltzmann model for simulating gas flow in kerogen pores. Transp Porous Media. 2015;106(2):285–301. https://doi.org/10.1007/s11242-014-0401-9.

Saarinen K. Color image segmentation by a watershed algorithm and region adjacency graph processing. In: Proceedings of the 1st international conference on image processing; 1994. https://doi.org/10.1109/ICIP.1994.413690.

Schembre JM, Kovscek AR. A technique for measuring two-phase relative permeability in porous media via X-ray CT measurements. J Pet Sci Eng. 2003;39(1):159–74. https://doi.org/10.1016/S0920-4105(03)00046-9.

Shabaninejad M, Middleton J, Fogden A. Systematic pore-scale study of low salinity recovery from Berea sandstone analyzed by micro-CT. J Pet Sci Eng. 2018;163:283–94. https://doi.org/10.1016/j.petrol.2017.12.072.

Shen WJ, Li XZ, Cihan A, Lu XB, Liu XH. Experimental and numerical simulation of water adsorption and diffusion in shale gas

reservoir rocks. Adv Geo-Energy Res. 2019;3(2):165–74. https://doi.org/10.26804/ager.2019.02.06.

Shewchuk JR. Delaunay refinement algorithms for triangular mesh generation. Comput Geom Appl. 2002;22(1):21–74. https://doi.org/10.1016/S0925-7721(01)00047-5.

Song FQ, Wang JD, Liu HL. Static threshold pressure gradient characteristics of liquid influenced by boundary wettability. Chin Phys Lett. 2010;27(2):024704. https://doi.org/10.1088/0256-307x/27/2/024704.

Song FQ, Song XX, Wang Y, Sun YH. Single- and two-phase flow model in low-permeability reservoir. Petroleum. 2019a;5(2):183–90. https://doi.org/10.1016/j.petlm.2018.05.004.

Song WH, Wang DY, Yao J, Li Y, Sun H, Yang YF, et al. Multiscale image-based fractal characteristic of shale pore structure with implication to accurate prediction of gas permeability. Fuel. 2019b;241:522–32. https://doi.org/10.1016/j.fuel.2018.12.062.

Song WH, Yao J, Li Y, Sun H, Zhang L, Yang YF, et al. Apparent gas permeability in an organic-rich shale reservoir. Fuel. 2016;181:973–84. https://doi.org/10.1016/j.fuel.2016.05.011.

Sparreboom W, van den Berg A, Eijkel JCT. Transport in nanofluidic systems: a review of theory and applications. New J Phys. 2010;12(1):015004. https://doi.org/10.1088/1367-2630/12/1/015004.

Sun H, Yao J, Cao YC, Fan DY, Zhang L. Characterization of gas transport behaviors in shale gas and tight gas reservoirs by digital rock analysis. Int J Heat Mass Transf. 2017;104:227–39. https://doi.org/10.1016/j.ijheatmasstransfer.2016.07.083.

Sun H, Yao J, Fan DY, Zhang L. Gas transport mode criteria in ultra-tight porous media. Int J Heat Mass Transf. 2015;83:192–9. https://doi.org/10.1016/j.ijheatmasstransfer.2014.11.075.

Tian XF, Cheng LS, Cao RY, An N, Zhang M, Wang Y. Characteristics of boundary layer in micro and nano throats of tight sandstone oil reservoirs. Chin J Comput Phys. 2016;33(6):717–24. https://doi.org/10.19596/j.cnki.1001-246x.2016.06.011 **(in Chinese)**.

Tian XF, Cheng LS, Cao RY, Wang Y, Zhao WQ, Yan YQ, et al. A new approach to calculate permeability stress sensitivity in tight sandstone oil reservoirs considering micro-pore-throat structure. J Pet Sci Eng. 2015;133:576–88. https://doi.org/10.1016/j.petrol.2015.05.026.

Wang S, Feng QH, Javadpour F, Zha M, Cui RH. Multiscale modeling of gas transport in shale matrix: an integrated study of molecular dynamics and rigid-pore-network model. SPE J. 2020. https://doi.org/10.2118/187286-PA.

Wang S, Javadpour F, Feng QH. Molecular dynamics simulations of oil transport through inorganic nanopores in shale. Fuel. 2016;171:74–86. https://doi.org/10.1016/j.fuel.2015.12.071.

Wu KL, Chen ZX, Li J, Li XF, Xu JZ, Dong XH. Wettability effect on nanoconfined water flow. Proc Natl Acad Sci. 2017;114(13):3358–63. https://doi.org/10.1073/pnas.1612608114.

Xiong W, Lei Q, Gao SS, Hu ZM, Xue H. Pseudo threshold pressure gradient to flow for low permeability reservoirs. Pet Explor Dev. 2009;36(2):232–6. https://doi.org/10.1016/S1876-3804(09)60123-3.

Yang YF, Yao J, Wang CC, Gao Y, Zhang Q, An SY, et al. New pore space characterization method of shale matrix formation by considering organic and inorganic pores. J Nat Gas Sci Eng. 2015;27:496–503. https://doi.org/10.1016/j.jngse.2015.08.017.

Yang YF, Wang K, Zhang L, Sun H, Zhang K, Ma JS. Pore-scale simulation of shale oil flow based on pore network model. Fuel. 2019;251:683–92. https://doi.org/10.1016/j.fuel.2019.03.083.

Yang YF, Li YW, Yao J, Iglauer S, Luquot L, Zhang K, et al. Dynamic pore-scale dissolution by CO_2-saturated brine in carbonates: impact of homogeneous versus fractured versus vuggy pore structure. Water Resour Res. 2020a;56(4):e2019WR026112. https://doi.org/10.1029/2019wr026112.

Yang YF, Tao L, Yang HY, Iglauer S, Wang X, Askari R, et al. Stress sensitivity of fractured and vuggy carbonate: an X-ray computed tomography analysis. J Geophys Res-Solid Earth. 2020b;125(3):e2019JB018759. https://doi.org/10.1029/2019jb018759.

Yang YF, Liu J, Yao J, Kou JL, Li Z, Wu TH, et al. Adsorption behaviors of shale oil in kerogen slit by molecular simulation. Chem Eng J. 2020c;387:124054. https://doi.org/10.1016/j.cej.2020.124054.

Yang ZM, Ma ZZ, Luo YT, Zhang YP, Guo HK, Lin W. A measured method for in situ viscosity of fluid in porous media by nuclear magnetic resonance. Geofluids. 2018;2018:8. https://doi.org/10.1155/2018/9542152.

Yao J, Sun H, Fan DY, Wang CC, Sun ZX. Numerical simulation of gas transport mechanisms in tight shale gas reservoirs. Pet Sci. 2013;10(4):528–37. https://doi.org/10.1007/s12182-013-0304-3.

Zeng BQ, Cheng LS, Li CL. Low velocity non-linear flow in ultra-low permeability reservoir. J Pet Sci Eng. 2011;80(1):1–6. https://doi.org/10.1016/j.petrol.2011.10.006.

Zhang K, Ma XP, Li YL, Wang CC. Parameter prediction of hydraulic fracture for tight reservoir based on micro-seismic and history matching. Fractals. 2018a;26(2):1–17. https://doi.org/10.1142/S0218348X18400091.

Zhang L, Jing WL, Yang YF, Yang HN, Guo YH, Sun H, et al. The investigation of permeability calculation using digital core simulation technology. Energies. 2019;12(17):3273. https://doi.org/10.3390/en12173273.

Zhang T, Li XF, Shi JT, Sun Z, Yin Y, Wu KL, et al. An apparent liquid permeability model of dual-wettability nanoporous media: a case study of shale. Chem Eng Sci. 2018b;187:280–91. https://doi.org/10.1016/j.ces.2018.05.016.

Zhang WM, Meng G, Wei XY. A review on slip models for gas microflows. Microfluid Nanofluid. 2012;13(6):845–82. https://doi.org/10.1007/s10404-012-1012-9.